Fast Lidar and Radar Multiple-Scattering Models. Part II: Wide-Angle Scattering Using the Time-Dependent Two-Stream Approximation

ROBIN J. HOGAN

Department of Meteorology, University of Reading, Reading, United Kingdom

ALESSANDRO BATTAGLIA

Meteorological Institute, University of Bonn, Bonn, Germany

(Manuscript received 5 October 2007, in final form 7 April 2008)

ABSTRACT

Spaceborne lidar returns from liquid water clouds contain significant contributions from photons that have experienced many wide-angle multiple-scattering events, resulting in returns appearing to originate from far beyond the end of the cloud. A similar effect occurs for spaceborne millimeter-wave radar observations of deep convective clouds. An efficient method is described for calculating the time-dependent returns from such a medium by splitting the photons into those that have taken a near-direct path out to and back from a single backscattering event (in the case of lidar, accounting for small-angle forward scatterings on the way, as described in Part I of this paper) and those that have experienced wide-angle multiple-scattering events. This paper describes the modeling of the latter using the time-dependent two-stream approximation, which reduces the problem to solving a pair of coupled partial differential equations for the energy of the photons traveling toward and away from the instrument. To determine what fraction of this energy is detected by the receiver, the lateral variance of photon position is modeled by the Ornstein–Fürth formula, in which both the ballistic and diffusive limits of photon behavior are treated; this is considerably more accurate than simple diffusion theory. By assuming that the lateral distribution can be described by a Gaussian, the fraction of photons within the receiver field of view may be calculated. The method performs well in comparison to Monte Carlo calculations (for both radar and lidar) but is much more efficient. This opens the way for multiple scattering to be accounted for in radar and lidar retrieval schemes.

1. Introduction

Part I of this paper (Hogan 2008, hereafter Part I) introduced the issue of radar and lidar multiple scattering in terms of four regimes. The first two are straightforward, and a very efficient method was introduced for treating the third of these, in which multiple scattering is dominated by small-angle forward scattering events. In this part, we consider the fourth regime, in which wide-angle multiple scattering becomes important. The particular difficulty to contend with is that the associated time delay makes returning photons appear to have originated from a range beyond the distance to which they actually penetrated, an effect known as "pulse stretching." This is particularly evident for spaceborne cloud lidar and radar because of the large detector footprint on the cloud: for lidar this occurs in observations of liquid water clouds (Platt and Winker 1995) and for 94-GHz radar it occurs in deep convective clouds (Battaglia et al. 2007).

There is potentially useful information available on the properties of clouds that can, in principle, be extracted from measurements subject to wide-angle multiple scattering. For example, the technique of "off-beam lidar" utilizes a single laser transmitter but a receiver array with a range of fields of view (Davis et al. 1999). The different degree of multiple scattering to which each field of view is sensitive allows the optical depth of liquid clouds to be estimated. Further information is available from depolarization measurements in the presence of multiple scattering (e.g., Sassen and Petrilla 1986), but polarization will not be treated in this paper.

Corresponding author address: Robin J. Hogan, Department of Meteorology, University of Reading, Earley Gate, P.O. Box 243, Reading RG6 6BB, United Kingdom.
E-mail: r.j.hogan@reading.ac.uk

DOI: 10.1175/2008JAS2643.1

The most rigorous method for interpreting measurements from active sensors is using a variational approach, in which a first guess of the profile of atmospheric properties is successively refined based on its ability to "forward model" the measurements. The difficulty with treating wide-angle multiple scattering is that until now there has been no forward model that is fast enough to use in a retrieval scheme. Monte Carlo methods have been used to model both lidar (Platt 1981) and radar (Battaglia et al. 2006) multiple scattering. Obviously these are not fast enough to use in a retrieval scheme directly, but Cahalan et al. (2005a) performed offline Monte Carlo simulations on a finite set of idealized cloud profiles and then constructed a retrieval that essentially searched for the simulation that best matched the observations. Although this approach benefits from the accuracy of the Monte Carlo calculations, the library of offline calculations clearly cannot represent all possible combinations of variables.

Other theoretical work used so far to interpret wide-angle multiple scattering has been based on diffusion theory (Davis et al. 1999; Davis and Marshak 2002), which is appropriate for very optically thick media in which photons rapidly lose memory of their initial direction. Although it has been applied to the exponential tails of the returns from optically thick clouds (Polonsky et al. 2005), it is not suited for more mixed profiles in which photons have a ballistic behavior in optically thinner regions and a diffusive behavior in optically thicker regions. More recently, Kobayashi et al. (2006) and Ito et al. (2007) developed an analytical model that includes pulse stretching, but only second-order scattering is included and the method is not fast enough to use in retrieval algorithms (Battaglia et al. 2008).

In this paper, a method is described that is accurate and efficient enough to use as a forward model in retrieval schemes both for radar and lidar multiple scattering. In section 2, an overview of the method is presented and the time-dependent two-stream (TDTS) approximation is introduced. In section 3, the contribution to apparent backscatter from those photons that have *not* experienced wide-angle scattering is calculated (i.e., regimes 1 or 2 in Part I). Then in section 4, the numerical integration of the time-dependent two-stream equations for calculating the wide-angle component is described. Comparison with Monte Carlo calculations is provided in section 5.

2. Overview of method

Although the method is applicable to both lidar and radar, the conventional unit for expressing the measured range-normalized intensity is different. For simplicity we use the usual lidar variable apparent backscatter $\hat{\beta}$ (in units of m^{-1} sr^{-1}) throughout the paper, defined as the backscatter coefficient of the medium that a measured intensity would correspond to in the absence of attenuation or multiple scattering (i.e., in regime 0 in the introduction of Part I). At radar wavelengths, the radar backscatter coefficient may be converted to an apparent radar reflectivity factor by the following (Donovan et al. 2001):

$$\hat{Z} = \frac{4}{|K_l|^2}\left(\frac{\lambda}{\pi}\right)^4 \hat{\beta}, \tag{1}$$

where $|K_l|^2$ is a reference dielectric factor of liquid water. Some calibration conventions use the value at centimeter wavelengths, 0.93, whereas others use the value at the frequency in question, but it should be noted that at millimeter wavelengths it is temperature dependent. See Hogan et al. (2006) for further discussion of radar calibration conventions.

The method is best described by reference to the space–time diagram in Fig. 1. The thick arrow indicates the outgoing quasi-direct beam, containing unscattered photons propagating away from the instrument at the speed of light c and, in the case of lidar, photons that have undergone small-angle forward scattering but are still considered to be part of the same beam. The cloud and aerosol profile is discretized into layers of thickness

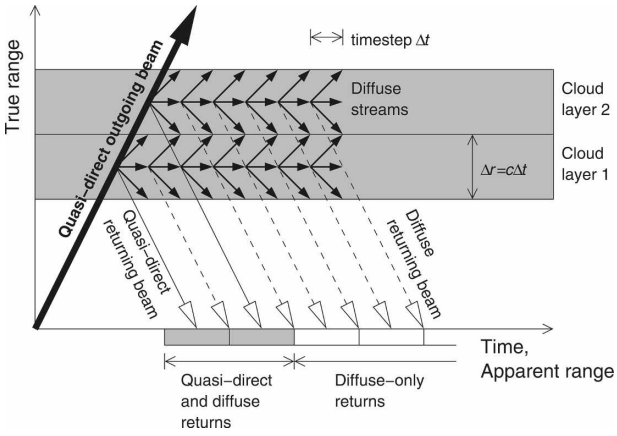

FIG. 1. Schematic space–time diagram illustrating the essentials of the algorithm. The thick arrow depicts the propagation of a transmitted beam toward a two-layer cloud. Some of the radiation is backscattered toward the receiver (solid open-headed arrows), and its travel time (distance on the abscissa) may be interpreted directly in terms of range to the layer. Some is scattered into diffuse streams inside the cloud, with the possibility of being subsequently scattered back toward the receiver (dashed open-headed arrows). In this case the travel time cannot be interpreted directly as a depth of penetration into the cloud.

Δr, which are assumed to be homogeneous in the directions perpendicular to the quasi-direct beam. It is also assumed that the pulse length is less than or equal to Δr. The very small fraction of photons in the quasi-direct beam that are backscattered toward the receiver can return to the instrument along a quasi-direct path (i.e., allowing for small-angle forward scattering on the return journey). They arrive at a time t (on the horizontal axis in Fig. 1) that may be unambiguously converted into the apparent range r using $r = 2ct$. Section 3 describes this part of the calculation, which uses the algorithm described in Part I or existing algorithms from the literature to derive the quasi-direct component of the apparent backscatter $\hat{\beta}^d$. However, the total apparent backscatter includes the contribution from wide-angle scattering $\hat{\beta}^w$, such that

$$\hat{\beta}(r) = \hat{\beta}^d(r) + \hat{\beta}^w(r). \tag{2}$$

To calculate $\hat{\beta}^w$, we consider the photons in the quasi-direct beam that experience wide-angle scattering within the cloud and then enter the diffuse distribution, which is modeled at each range gate by an outgoing and an incoming stream $I^{\pm}$ traveling in two discrete directions. Their evolution is governed by the time-dependent two-stream equations

$$\frac{1}{c}\frac{\partial I^+}{\partial t} = -\mu_1 \frac{\partial I^+}{\partial r} - \mu_1 \alpha(\gamma_1 I^+ - \gamma_2 I^-) + S^+, \tag{3}$$

$$\frac{1}{c}\frac{\partial I^-}{\partial t} = +\mu_1 \frac{\partial I^-}{\partial r} - \mu_1 \alpha(\gamma_1 I^- - \gamma_2 I^+) + S^-, \tag{4}$$

where the coefficients γ_1 and γ_2 are given by

$$\gamma_1 = [1 - \tilde{\omega}(1 + g)/2]/\mu_1, \tag{5}$$

$$\gamma_2 = \tilde{\omega}(1 - g)/(2\mu_1), \tag{6}$$

and the medium is described by the standard range-dependent quantities extinction coefficient α, single-scattering albedo $\tilde{\omega}$, and asymmetry factor g. The cosine of the angle between these streams and the outgoing direction is $\pm\mu_1$, such that the streams propagate away from the instrument at a speed $\pm\mu_1 c$. The two streams are represented in Fig. 1 by the short 45° arrows; note that the short horizontal arrows simply represent the fraction of the diffuse radiation that does not leave a particular layer within the time step Δt.

It can be seen that (3) and (4) are simply the standard time-independent two-stream equations with the addition of a time derivative on the left-hand side. The time-independent form is used in the radiation schemes of almost all weather forecast and climate models (e.g., Meador and Weaver 1980; Zdunkowski et al. 1982; Edwards and Slingo 1996; Stephens et al. 2001; Shonk and Hogan 2008), where the equations are solved as a boundary value problem. In modeling the propagation of a short pulse of radiation, we simply add the time-derivative terms to yield a pair of coupled partial differential equations, which are solved as an initial value problem. The time-dependent two-stream equations have appeared before (Durian and Rudnick 1997), but to the authors' knowledge, their only previous atmospheric use was by Ayoubi and Nelson (1989), who tackled the lidar multiple scattering problem but only in the small-angle limit.

The terms on the right-hand side of (3) and (4) each have a straightforward interpretation. The first represents radiative transport from one range gate to another and is analogous to the advection term in the Navier–Stokes equations of fluid dynamics. The second term represents the loss of energy from a stream by scattering and absorption (governed by γ_1) and the gain of energy by scattering from the other stream (governed by γ_2). The final terms $S^{\pm}$ are functions of both r and t and represent the source of energy from the quasi-direct beam. Calculation of the source terms is analogous to a short-wave time-independent two-stream radiation scheme, in which the direct solar beam propagates down through the atmosphere and at each height the component that is scattered forms the source terms for the two-stream equations, which then estimate the diffuse fluxes as a function of height. In the present case, the lidar or radar transmitter performs the same role as the sun. Section 3 describes how the source terms are calculated; section 4 describes how (3) and (4) are numerically integrated forward in time.

3. Calculation of the quasi-direct component and the source terms for the diffuse calculation

a. Radar: Single scattering

For radar observations of clouds and precipitation, in which the diameter of the largest particles is, at most, of the same order as the wavelength, the quasi-direct component of the apparent backscatter $\hat{\beta}^d$ is described simply by the lidar equation [provided as Eq. (1) in Part I]. As explained by Hogan (2006), if range gate i represents ranges from r_i to $r_i + \Delta r$ (over which the backscatter coefficient β_i and extinction coefficient α_i are constant) then the apparent backscatter averaged across the gate is

$$\hat{\beta}_i^d = \hat{\beta}_i \exp[-2\delta(r_i)] \frac{1 - \exp(-2\alpha_i \Delta r)}{2\alpha_i \Delta r}, \tag{7}$$

where $\delta(r) = \int_0^r \alpha \, dr$ is the optical depth of the medium to range r from the transmitter.

The next step is to calculate the source terms for the diffuse calculation. The diffuse radiances in each direction $I^{\pm}_{i,j}$ are normalized such that they represent the fraction of the initial transmitted energy that is present in a particular gate i in a particular time step j in a particular direction. Therefore, the source terms S_i^+ and S_i^- represent the fraction of the total transmitted energy that enters the outgoing and incoming diffuse beams, respectively, at range gate i at time r_i/c after the pulse is transmitted. First, the average transmission to gate i, $\mathcal{T}_i$, is calculated, which is simply the one-way equivalent of the transmission part of (7):

$$\mathcal{T}_i = \exp[-\delta(r_i)][1 - \exp(-\alpha_i \Delta r)](\alpha_i \Delta r)^{-1}. \quad (8)$$

The fraction of the initial energy scattered into the diffuse distribution at gate i is therefore $\tilde{\omega}_i \alpha_i \mathcal{T}_i$, where $\tilde{\omega}$ is the single-scattering albedo of the medium. To determine what fraction enters the outgoing stream and what fraction enters the incoming stream, we make use of the Eddington phase function. In the case of scattering from the outgoing beam ($\mu = 1$) into the two streams ($\mu = \pm\mu_1$), this predicts the azimuthally averaged phase function $p(1, \pm\mu_1) = 1 \pm 3g\mu_1$, where g is the asymmetry factor of the medium. Thus, the source terms at gate i are given by

$$S_i^{\pm} = \tilde{\omega}_i \alpha_i \mathcal{T}_i (1 \pm 3g_i \mu_1)/2. \quad (9)$$

The factor of 2 in the denominator is due to the normalization of the phase function and ensures that in a nonabsorbing cloud ($\tilde{\omega}=1$) with infinite optical depth, the sum of all the source terms is unity, indicating that all the incident radiation ends up in the diffuse distribution. For $g > 1/3\mu_1$, (9) results in the unphysical $S^- < 0$, so instead in this instance we would use $S_i^+ = \tilde{\omega}_i \alpha_i \mathcal{T}_i$ and $S_i^- = 0$. In practice this does not occur for radar because the particles are too small, whereas for lidar the forward lobe in the phase function means that it is appropriate to first apply a scaling (as described in section 3b), which reduces g below $1/3\mu_1$.

The final step is to calculate the spatial variance of the radiation in the unscattered beam when it reaches gate i, which is discussed in section 4b. We denote the distance of an individual photon from the axis of the instrument as s. If the transmitted photon distribution from the instrument may be described as a Gaussian with a $1/e$ angular half-width of $\rho_{\rm tr}$, then the variance of the spatial distribution at range r is simply

$$\overline{s^2}_d = \rho_{\rm tr}^2 r^2, \quad (10)$$

which is the same as Eq. (5) in Part I but with a subscript d to denote the quasi-direct distribution of photons, to contrast with the wide-angle distribution described in section 4b.

b. Lidar: Small-angle multiple scattering

When the characteristic size of the scatterers is much larger than the wavelength of the radiation, as is the case in most lidar cloud remote sensing, half of the photons that interact with a scatterer will be diffracted around the particle, forming a narrow "forward-scattering lobe" in the phase function, as discussed in detail in Part I. The remaining half intercept the particle and are then either scattered into a wide distribution of angles (forming the large-angle component of the phase function) or absorbed. We treat the forward-scattered photons as being part of the "quasi-direct beam," behaving almost if they had not been scattered at all.

To determine the apparent backscatter due to the quasi-direct beam $\hat{\beta}^d$, we use the "photon variance–covariance" (PVC) approach described in Part I. By calculating the variance and covariance of photon position and direction as a function of range, it efficiently includes photons that have been forward-scattered an arbitrary number of times on the outgoing or return journeys. Two versions are available: that of Hogan (2006), which is $O(N^2)$ efficient for a profile defined by N points, or the more recent version described in Part I, which achieves $O(N)$ efficiency with only a slight decrease in accuracy.

To describe what happens to the widely scattered photons, it is appropriate to define what will be referred to as "diffraction-scaled" values for the extinction coefficient, single-scattering albedo, and asymmetry factor:

$$\alpha'' = \alpha/2, \quad (11)$$

$$\tilde{\omega}'' = 2\tilde{\omega} - 1, \quad (12)$$

$$g'' = g + (g - 1)/\tilde{\omega}''. \quad (13)$$

This transformation is analogous to the delta-Eddington scaling (Joseph et al. 1976) used in section 4, but it is more appropriate here when we wish only to remove the narrow forward lobe that has already been dealt with by the PVC model, not the often larger fraction of the forward phase function that is removed by delta-Eddington scaling.[1] In deriving (12) we have assumed

[1] Joseph et al. (1976) actually derived general scaling equations in terms of the fraction f of the scattered energy that is in the forward lobe. They then assumed $f = g^2$ to obtain delta-Eddington scaling. The diffraction scaling of (11)–(13) may be obtained from their general equations by instead setting $f = (2\tilde{\omega})^{-1}$.

that, as in Mie theory, an absorbing particle only absorbs photons that are directly intercepted by it, not those that are diffracted into the forward lobe. Therefore, the minimum value of $\tilde{\omega}$ represented satisfactorily by this approach is 0.5 (for which $\tilde{\omega}''=0$). Likewise, to prevent negative values of g'' it is necessary that $g > (2\tilde{\omega})^{-1}$.

At each range gate, these values are combined with the corresponding unscaled values for molecular scattering and absorption and then used to calculate a scaled optical depth $\delta(r)$ for use in calculating the transmission and source terms using (8) and (9). It should be noted that both delta-Eddington-scaled and diffraction-scaled values have been tried in the algorithm, but only diffraction scaling provided satisfactory agreement with Monte Carlo calculations. It should be stressed that diffraction scaling is only used in (8) and (9), not in the subsequent treatment of the radiation where standard delta-Eddington scaling is used (e.g., in sections 4a and 4c).

For lidar, the calculation of $\overline{s^2}_d$, the spatial variance of the photons in the quasi-direct beam, needs to include not only the unscattered photons described by (10) but also the broadening effect caused by the contribution from the forward-scattered photons. This may be achieved using the procedure described in section 2b of Part I, but without the use of the equivalent medium theorem (hence, $\overline{s^2}_d$ is not identical to the variable $\overline{s^2}$ used in Part I).

4. Calculation of the diffuse component

This section describes the derivation of $\hat{\beta}^w$, the contribution to the backscatter from the photons that have experienced wide-angle multiple scattering. First, in section 4a, the TDTS equations are used to estimate the diffuse radiances in each direction as a function of time and range from the instrument. Second, because the photons spread out laterally, we need to calculate what fraction of this energy remains within the instrument field of view. This is achieved in section 4b by modeling the lateral spatial variance of photon position using essentially the same equations. Finally in section 4c, the receiver pattern is used to estimate the intensity of the returned radiation as a function of time.

a. Integration of the time-dependent two-stream equations

Equations (3) and (4) are integrated on a discrete grid in time and space, where for convenience the time step Δt is related to the grid spacing Δr (assumed to be regular) by $\Delta t = \Delta r/c$. This ensures that in one time step the quasi-direct beam will travel a distance Δr, whereas in the optically thin limit the diffuse streams will travel $\pm\mu_1\Delta r$. Several different values for μ_1 have been proposed in the literature (Meador and Weaver 1980), but in this application, the best a posteriori agreement with Monte Carlo calculations is found for $\mu_1 = 1/2$ (e.g., Toon et al. 1989).

For lidar observing particles much larger than the wavelength, the standard delta-Eddington scaling (Joseph et al. 1976) is used to account for the narrow forward lobe in the phase function, and all further use of these variables in the context of lidar refers to the delta-Eddington-scaled versions. For radar, the particles are at most of a similar scale to the wavelength of the radiation, so no delta-Eddington scaling is applied.

To solve (3) and (4), we first consider the case for $\mu_1\alpha\gamma_2 c\Delta t \ll 1$, which corresponds to the limit at which the probability of a photon being scattered into the other direction within a single time step is much less than unity. In this limit we can discretize (3) using an explicit forward time step and the spatial derivative using a simple upstream scheme. Although it is known that the first-order upstream scheme is numerically diffusive, this is actually a desirable property because in reality the radiation is not all traveling at the discrete speeds $\pm\mu_1 c$ in the r direction. So if $I^+_{i,j}$ represents the outgoing radiance at range gate i and time step j, then the radiance at the subsequent time step is given by

$$I^+_{i,j+1} = I^+_{i,j} + c\Delta t[\mu_1(I^+_{i-1,j} - I^+_{i,j})/\Delta r - \mu_1\alpha(\gamma_1 I^+_{i,j} - \gamma_2 I^-_{i,j}) + S^+_{i,j}], \quad (14)$$

and similarly for $I^-_{i,j+1}$. The radiances are initialized to zero, and hence the energy enters the system purely through the source terms $S^{\pm}_{i,j}$. Because the time step is such that the direct beam travels exactly one range gate in one time step, $S^{\pm}_{i,j}$ is only nonzero when $i = j$.

When $\mu_1\alpha\gamma_2 c\Delta t$ exceeds unity, the simple discretization of (14) cannot be used because it predicts that more radiation is transferred to the other stream than is actually present, leading to numerical instability. The problem is that many scattering events may occur within a single time step, so the system represented by the coupled partial differential Eqs. (3) and (4) has become "stiff." A solution is to define six coefficients at each range gate, Δ^0_i to Δ^5_i, expressing what fraction of the energy in $I^+_{i,j}$ is transferred into adjacent range gates (or remains at the same range gate in the case of Δ^0_i) in a single time step. In this way, the forward step is implemented by

$$I^+_{i,j+1} = \Delta^0_i I^+_{i,j} + \Delta^1_i I^-_{i,j} + \Delta^2_{i-1} I^+_{i-1,j} + \Delta^3_{i+1} I^-_{i+1,j} + \Delta^4_{i+1} I^+_{i+1,j} + \Delta^5_{i-1} I^-_{i-1,j} + c\Delta t S^+_{i,j}, \quad (15)$$

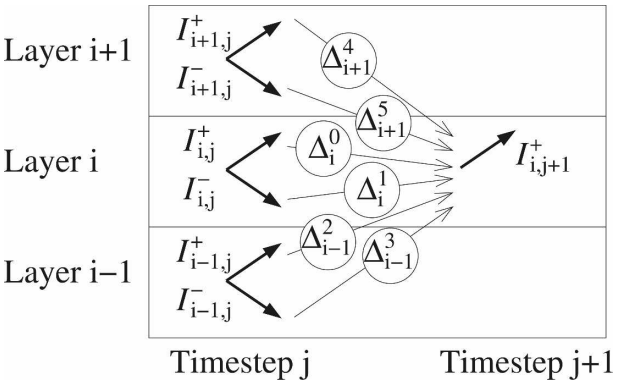

FIG. 2. Schematic illustrating how coefficients Δ^0 to Δ^5 in (15) control how the outgoing radiance $I^+_{i,j+1}$ at time step $j + 1$ is determined by the radiances in adjacent layers at time step j.

and similarly for $I^-_{i+1,j}$. This is illustrated in Fig. 2. The coefficients are defined once for a given profile, including the possibility of multiple scattering within a single time step. The calculation of these coefficients is described in the appendix.

b. The variance of the photon distribution

To describe the rapid lateral spreading of the photon distribution with time, we need to model the spatial variances of the photon distribution $\overline{s^2}^{\pm}_w$ (the subscript w denotes photons arising from wide-angle scattering, as distinct from $\overline{s^2}_d$). In the case in which diffusion theory is applicable, one would expect the evolution of the spatial variance in an infinite medium to be governed by

$$\partial \overline{s^2}_w / \partial t = 4D, \tag{16}$$

where D is the diffusivity of the medium. This result is from classical diffusion theory, originally derived by Einstein in 1905 (Einstein 1956). The prefactor of 4 corresponds to expansion in two spatial dimensions, whereas for expansion in one or three dimensions the prefactor would be 2 or 6, respectively. In radiative transfer, the diffusivity is given by (Durduran et al. 1997; Davis and Marshak 2001)

$$D = c l_t / 3, \tag{17}$$

where l_t is the transport mean-free path:

$$l_t = [\alpha(1 - \tilde{\omega} g)]^{-1}. \tag{18}$$

However, as recognized by Einstein, diffusion theory is not applicable until a number of scattering events have taken place; if (17) is substituted directly into (16) then it can be shown that the initial evolution of the variance implies faster-than-light travel. A more accurate description can be obtained using the Langevin equation, which predicts the statistics of particles in Brownian motion. Ornstein and Fürth independently used this approach to derive the positional variance of such particles as a function of time (Uhlenbeck and Ornstein 1930). By drawing an analogy between Brownian motion and a photon undergoing multiple scattering [e.g., by replacing the mean particle speed with the speed of light (Gopal et al. 2001)], we may write the resulting Ornstein–Fürth formula in the language of radiation transport:

$$\overline{s^2}_w = \overline{s^2}_d + \frac{4}{3} l_t^2 (\overline{n} + e^{-\overline{n}} - 1), \tag{19}$$

where $\overline{s^2}_d$ is the initial spatial variance and $\overline{n} = ct/l_t$ is the effective mean number of scattering events after time t. Note that as with (16), the factor 4 in (19) may be replaced by 2 or 6 to represent the evolution of the positional variance in one or three dimensions, respectively. It is easy to show that in the limit of many scattering events ($\overline{n} \gg 1$), the time derivative of $\overline{s^2}_w$ follows diffusion theory as described by (16) and (17), whereas in the limit of few scattering events $\overline{n} \gg 1$), we have $\partial(\overline{s^2}_w)^{1/2}/\partial t \simeq (2/3)^{1/2} c$. This latter case corresponds to a spherical shell of unscattered photons expanding out at the speed of light from their point of origin.

To test the validity of (19) for radiation, simple Monte Carlo calculations have been carried out in which a distribution of photons is initialized within an infinite, homogeneous cloud of isotropic scatterers and the photon trajectories are modeled over time. The initial distribution is assumed to be Gaussian in the x and y directions (centered at $x = y = 0$) and a delta function in the orthogonal r direction (at $r = 0$), with a random initial direction. This approximately represents photons that have been scattered from the quasi-direct beam into the diffuse distribution, as described in section 3. Figure 3 shows the evolution of the spatial variance $\overline{s^2}_w = \overline{x^2} + \overline{y^2}$ with time, with both axes normalized to make the results applicable to a medium with any value of l_t. It can be seen that (19) provides an excellent fit to the Monte Carlo results for a cloud of infinite optical depth. Direct application of diffusion theory, however, tends to strongly overestimate the variance at early times. Figure 3 shows the case for an initial spatial variance of $\overline{s^2}_d = 0$, but the same results are found for nonzero values, which has the effect of simply moving the lines upward. The deficiencies of diffusion theory after only a few scattering events were noted also by Platnick (2001); he fitted empirical relationships to his Monte Carlo calculations, but they performed less well than the Ornstein–Fürth formula does in Fig. 3.

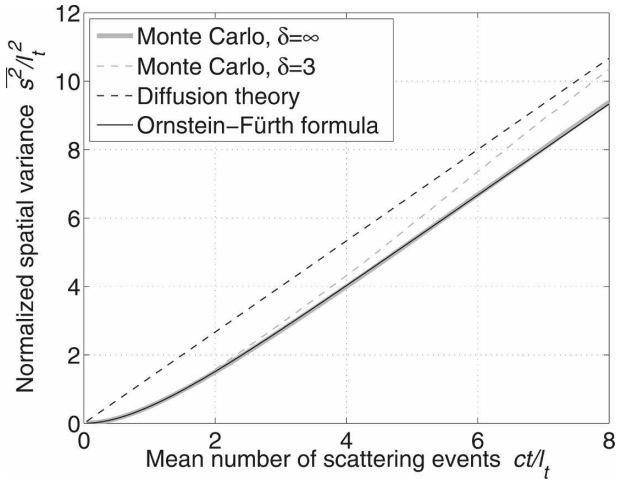

FIG. 3. Monte Carlo calculation of the evolution of the variance of photon position in the x and y directions from an initial value of $\overline{s^2}_d = 0$. Scattering is isotropic and the results are plotted against the mean number of scattering events $\bar{n} = ct/l_t$. The thick gray line corresponds to Monte Carlo calculations in an infinite domain, whereas the thin dashed gray line considers a cloud that is finite in the r direction (orthogonal to x and y) with an optical depth $\delta = 3$. The photons are initialized in the center of the cloud in the r direction, and those that escape are not considered in the calculation of the spatial variance. Also shown is the prediction of diffusion theory [Eqs. (17) and (18)] and the Ornstein–Fürth formula [Eq. (19)]. The Monte Carlo calculations used 2×10^4 photons.

The discussion so far in this section has considered only horizontal transport. To account for the transport of photon variance from one gate and one stream to another, we consider the energy-weighted variances $J^+ = I^+\overline{s^2}^+_w$ and $J^- = I^-\overline{s^2}^-_w$. The evolution of these quantities may be described in exactly the same way as the diffuse radiances, as follows:

$$\frac{1}{c}\frac{\partial J^+}{\partial t} = -\mu_1 \frac{\partial J^+}{\partial r} - \mu_1 \alpha(\gamma_1 J^+ - \gamma_2 J^-) + S^+ \overline{s^2}_d + I^+ \left.\frac{\partial \overline{s^2}^+_w}{\partial t}\right|_{\text{diff}}, \tag{20}$$

$$\frac{1}{c}\frac{\partial J^-}{\partial t} = +\mu_1 \frac{\partial J^-}{\partial r} - \mu_1 \alpha(\gamma_1 J^- - \gamma_2 J^+) + S^- \overline{s^2}_d + I^- \left.\frac{\partial \overline{s^2}^-_w}{\partial t}\right|_{\text{diff}}. \tag{21}$$

These are essentially the same as (3) and (4), except that the source term from the quasi-direct beam also includes its variance $\overline{s^2}_d$, and an additional source term appears as a result of a diffusion-like process in the horizontal.

In terms of discretization, (20) and (21) may be treated in exactly the same way as (3) and (4), using an equation analogous to (15) with the same coefficients. When required, the variances may be recovered by dividing through by the diffuse radiances: $\overline{s^2}^{\pm}_w = J^{\pm}/I^{\pm}$. To discretize the final term of (20) and (21), we need to be able to estimate $\bar{n}$ at time step j from each of $\overline{s^2}^+_w$ and $\overline{s^2}^-_w$. Unfortunately, (19) cannot be inverted directly, so instead we make a first guess by inverting one of the two asymptotic forms for $\bar{n}$, depending on the value of $(\overline{s^2}_w - \overline{s^2}_d)/l_t^2$:

$$\begin{aligned}(\overline{s^2}_w - \overline{s^2}_d)/l_t^2 &= (2/3)\bar{n}^2;\ (\overline{s^2}_w - \overline{s^2}_d)/l_t^2 < 0.8,\\ (\overline{s^2}_w - \overline{s^2}_d)/l_t^2 &= (4/3)(\bar{n} - 1);\ (\overline{s^2}_w - \overline{s^2}_d)/l_t^2 \geq 0.8.\end{aligned} \tag{22}$$

One step of Newton's method in log–log space is sufficient to obtain an accurate value at time step j, $\bar{n}_j$. At the next time step, the mean number of scattering events will be $\bar{n}_{j+1} = \bar{n}_j + c\Delta t/l_t$. We can therefore use (19) to obtain

$$\left.\frac{\partial \overline{s^2}_w}{\partial t}\right|_{\text{diff}} = \frac{\overline{s^2}_{w,j+1} - \overline{s^2}_{w,j}}{\Delta t} = \frac{4l_t^2}{3\Delta t}(\bar{n}_{j+1} - \bar{n}_j + e^{-\bar{n}_{j+1}} - e^{-\bar{n}_j}). \tag{23}$$

This is applied in (20) and (21) at each range gate and each time step.

As a final point, it should be noted that despite the good fit to the Monte Carlo results in Fig. 3, other factors can limit the accuracy of (19). In particular, in an optically thin cloud, the photons that escape from the top or bottom of the cloud will preferentially be those with a smaller lateral variance, with the result that those photons that remain in the cloud will tend to have a larger lateral variance than would be expected in an infinite cloud. To illustrate this, the dashed line in Fig. 3 shows a Monte Carlo calculation for a cloud with an optical depth of $\delta = 3$; it can be seen that as the number of scattering events increases, (19) increasingly underestimates the lateral variance. However, as δ increases, the behavior quickly approaches that for $\delta = \infty$. One way to represent the δ-dependence could be to multiply the first term on the right-hand side of (20) and (21) by a factor between 0 and 1, thereby representing the fact that the photons that are transported in the direction r tend to be those that have a lower variance in the x and y directions. Alternatively, l_t could be artificially increased near cloud boundaries so that the rate of increase of variance predicted by (23) would be larger. However, appropriate theory would have to be developed to parameterize these changes in terms of variables available to the TDTS method.

c. Calculation of apparent backscatter

The final step is to calculate the apparent backscatter due to wide-angle scattering $\hat{\beta}^w$ by considering the fraction of photons at each range gate and time step that is scattered directly back toward the receiver and detected (i.e., applying the formal solution for the fluxes to obtain the radiance in the direction of the instrument). This involves convolving the photon distribution with the receiver pattern and accounting for losses on the return journey. The apparent backscatter component due to scattering from the diffuse photon distribution at range gate i and time step j, traveling away from (+) and toward (−) the receiver, is given by

$$\Delta\hat{\beta}_{i,j}^{\pm} = \frac{\tilde{\omega}_i \alpha_i \mathcal{T}_i (1 \mp 3 g_i \mu_1)}{4\pi} \times \frac{\int_0^\infty E_{i,j}^{\pm}(s) R_i(s) s \, ds}{\int_0^\infty T_i(s) R_i(s) s \, ds}, \tag{24}$$

where the first term on the right-hand side represents the probability that photons are scattered toward the receiver and accounts for the transmission on the return journey. It can be derived in an analogous way to the source term given by (9), but note that in the case of lidar we here use the usual delta-Eddington-scaled values rather than the diffraction-scaled values. The factor of 4π in the denominator ensures that apparent backscatter is expressed as the fraction of the transmitted energy per unit of path that is returned per steradian in the backscatter direction (i.e., it has units of $\mathrm{m}^{-1}\ \mathrm{sr}^{-1}$; $I^{\pm}$ and $E^{\pm}$ are not normalized in this way). The second term on the right consists of a convolution of the photon distribution $E^{\pm}(s)$ with the receiver pattern $R(s)$, where s is again the lateral distance from the receiver axis. This is normalized by a convolution of the transmitter pattern $T(s)$ with the receiver pattern so that the multiply scattered return is scaled correctly with respect to the unscattered return.

We assume that the transmitter pattern and the lateral photon distributions can be described by Gaussians as follows:

$$T_i(s) = \frac{1}{\pi \rho_{\mathrm{tr}}^2 r_i^2} \exp\left(-\frac{s^2}{\rho_{\mathrm{tr}}^2 r_i^2} \right), \tag{25}$$

$$E_i^{\pm}(s) = \frac{I^{\pm}}{\pi \overline{s^2}_w^{\pm}} \exp\left(-\frac{s^2}{\overline{s^2}_w^{\pm}} \right). \tag{26}$$

Note that the transmitter pattern is normalized so that its integral over all s is unity; that is, $2\pi\int_0^\infty T_i(s) s \, ds = 1$. The assumption of a Gaussian lateral photon distribution is valid after many multiple-scattering events, as well as at early times when scattered photons have not traveled far compared to the width of the Gaussian transmitter pattern. In other cases it is less valid (e.g., Durian and Rudnick 1997). More precise estimation of the distribution shape could be achieved by using the approach in section 4b to model moments of the distribution other than the second, but the performance of the Gaussian approximation in the next section suggests that this additional level of complexity is not justified.

The receiver pattern may be described by either a Gaussian (appropriate for a radar antenna) or a "top-hat" function (appropriate for a lidar telescope). In the former case, when the same antenna is used for transmission and reception, the receiver pattern is the same; i.e., $R_i = T_i$. Substitution of these functions into (24) yields

$$\Delta\hat{\beta}_{i,j}^{\pm} = \frac{\tilde{\omega}_i \alpha_i \mathcal{T}_i (1 \mp 3 g_i \mu_1)}{4\pi} \times \frac{2 I_i^{\pm}}{1 + \overline{s^2}_{w,i}^{\pm} / (\rho_{\mathrm{fov}} r_i)^2}. \tag{27}$$

In the case of a lidar, the receiver pattern may be represented by

$$R_i(s) = \begin{cases} 1/\pi\rho_{\mathrm{fov}}^2; & s \le \rho_{\mathrm{fov}} \\ 0; & s > \rho_{\mathrm{fov}} \end{cases}, \tag{28}$$

which results in

$$\Delta\hat{\beta}_{i,j}^{\pm} = \frac{\tilde{\omega}_i \alpha_i \mathcal{T}_i (1 \mp 3 g_i \mu_1)}{4\pi} \times I_i^{\pm} \frac{1 - \exp(-\rho_{\mathrm{fov}}^2 r_i^2 / \overline{s^2}_{w,i}^{\pm})}{1 - \exp(\rho_{\mathrm{fov}}^2 / \rho_{\mathrm{tr}}^2)}. \tag{29}$$

The wide-angle apparent backscatter is calculated by summing up the appropriate values of $\Delta\hat{\beta}_{i,j}^{\pm}$. The complication is that although apparent backscatter is output on the same grid as the input variables (α_i, $\tilde{\omega}_i$, and g_i), the time step j must be taken into account because it leads to returns appearing to originate farther from the instrument. This is best explained with reference to Fig. 1: to work out the returned power at a particular "apparent" range on the abscissa, we must sum up the contributions from each range gate and time step along the diagonal path of the returning beams. The result is that radiation scattered toward the receiver from a given combination of range gate i and time step j will appear to have originated from a range $r = r_i + (j - i)c\Delta t/2$. In terms of measured backscatter due to wide-angle multiple scattering $\hat{\beta}^w$ at an apparent range gate k, we have the following summation:

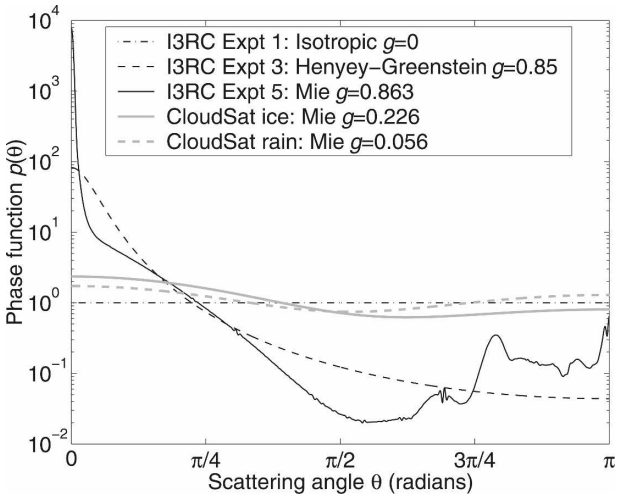

FIG. 4. Scattering phase functions used in section 5 to test the multiple scattering model: lidar phase functions from the I3RC, in which the Mie phase function is for a distribution of liquid droplets with an effective radius of 10 μm observed by a 532-nm lidar (black lines), and 94-GHz radar phase functions for individual ice spheres of diameter 1 mm and liquid spheres of diameter 0.8 mm (gray lines).

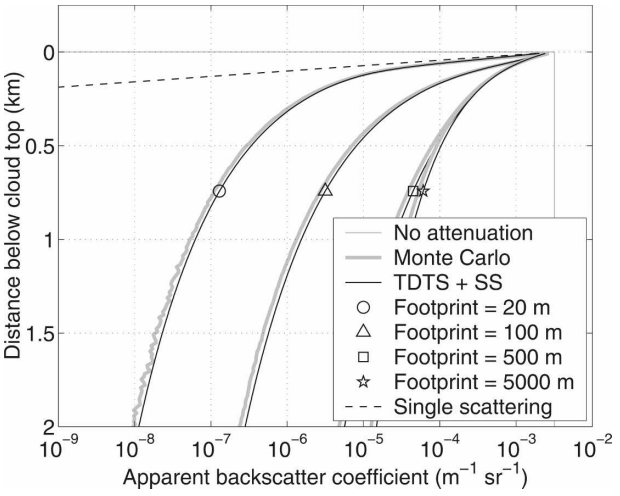

FIG. 5. Comparison of apparent backscatter vs the apparent distance below cloud top for experiment 1 of I3RC (phase III, case 7), which consists of a semi-infinite cloud of nonabsorbing isotropic scatterers, as described in section 5a. The thick gray lines show the calculations of the Monte Carlo model of Battaglia et al. (2006); the solid black lines show the results for the new method, in this case using a combination of the TDTS method and single scattering (SS).

$$\hat{\beta}_k^w = \sum_{n=1}^{k} \Delta\hat{\beta}^+_{n,2k-n} + \Delta\hat{\beta}^+_{n,2k-n+1} + \Delta\hat{\beta}^-_{n,2k-n} + \Delta\hat{\beta}^-_{n,2k-n+1}. \quad (30)$$

Finally, this wide-angle apparent backscatter must be added to the quasi-direct backscatter to obtain the total apparent backscatter [Eq. (2)].

5. Comparison against Monte Carlo calculations

In this section, the fast multiple scattering model developed in this paper will be compared to the Monte Carlo model of Battaglia et al. (2006) for both lidar and radar cases.

a. Spaceborne lidar

Three of the experiments from the Intercomparison of 3D Radiation Codes (I3RC, Cahalan et al. 2005b) are used to demonstrate the ability of the model to represent different kinds of phase functions, as shown by the black lines in Fig. 4. The first profile (experiment 1 of I3RC; phase III, case 7) considers a semi-infinite horizontally homogeneous cloud with an extinction coefficient of 0.04 m^{-1} that is illuminated by an instantaneous pulse of photons with zero lateral width in a direction normal to the plane of the cloud. The scatterers are assumed to be isotropic ($g = 0$) and nonabsorbing ($\tilde{\omega} = 1$).

To model the backscatter measured from this cloud, we use a combination of single scattering (regime 1 in Part I) and wide-angle scattering modeled by the TDTS method (regime 3 in Part I). A range-gate spacing of 15 m is used, and the receiver is assumed to have a top-hat response function. Figure 5 shows the apparent backscatter as a function of apparent range below cloud top for three receiver fields of view, corresponding to footprints with diameters between 20 and 5000 m. Good agreement can be seen between the Monte Carlo and the TDTS for all fields of view, although in common with all the lidar comparisons in this section, the TDTS model appears to overestimate the backscatter to a modest degree.

Figure 6 compares the total energy of the diffuse photons within the cloud as a function of time and distance below cloud top (in the case of the TDTS model the total energy is simply $I^+ + I^-$). The diagonal edge to the top left of each panel corresponds to the incoming direct beam traveling at the speed of light. Good agreement is evident between TDTS and Monte Carlo, with the photon concentrations decreasing rapidly beyond a depth of 0.5–1 km into the cloud. Thus, the apparent backscatter values that appear to have originated from deep in the cloud in Fig. 5 are actually predominantly from photons that penetrate only a few hundred meters below cloud top. Figure 7 depicts the corresponding root-mean-square (RMS) horizontal displacement of the photons within the cloud. The first

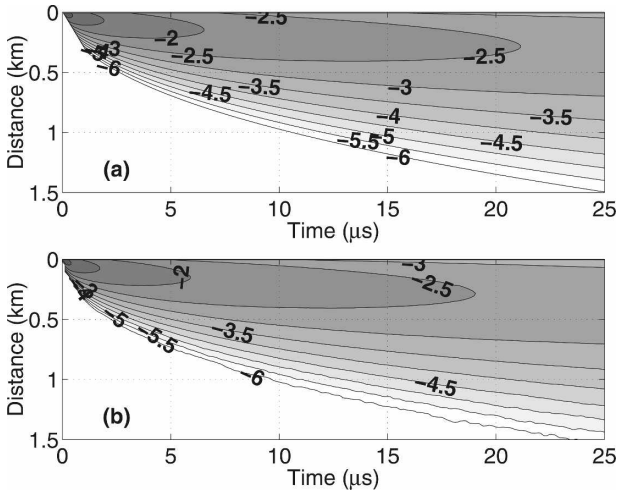

FIG. 6. The base-10 logarithm of the total diffuse radiative energy in a given level as a function of time and true distance below cloud top for the lidar profile shown in Fig. 5, calculated by (a) the TDTS model and (b) the Monte Carlo model. Thus, in the case of the TDTS model, the quantity shown is $\log_{10}(I^+ + I^-)$.

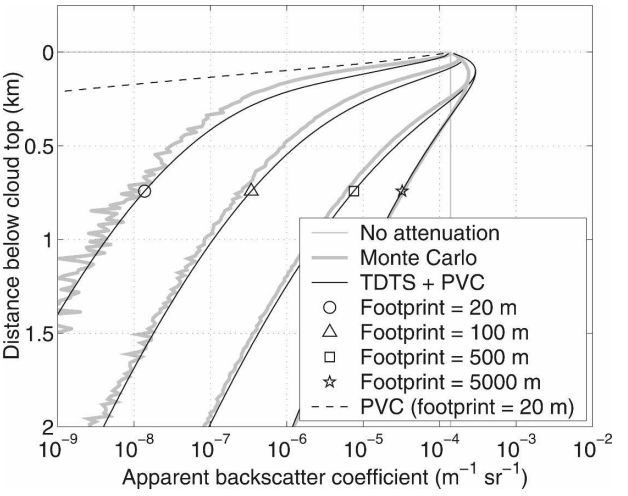

FIG. 8. As Fig. 5, but for the second profile described in section 5a (experiment 3of I3RC; phase III, case 7). This consists of a semi-infinite cloud of absorbing particles with a single scattering albedo of $\tilde{\omega} = 0.98$ and the Henyey–Greenstein phase function shown in Fig. 4.

thing to note is that where the total diffuse radiative energy in Fig. 6 falls below around 10^{-5}, the Monte Carlo calculation simulates too few photons to estimate the RMS displacement accurately. However, where the energy is larger, good agreement is found, lending support to the use of the Ornstein–Fürth formula described in section 4b.

The second profile (experiment 3 of I3RC; phase III, case 7) considers the same semi-infinite cloud as in the first profile, but with a single-scattering albedo of $\tilde{\omega} = 0.98$ and a Henyey–Greenstein phase function with $g = 0.85$, as illustrated by the black dashed line in Fig. 4. The cloud is illuminated by a point source of photons as before. This case is modeled by a combination of small-angle multiple scattering using the photon variance–covariance method of Hogan (2006) and the TDTS method. The PVC method describes the forward lobe as a Gaussian with a $1/e$ half-width of $\Theta = 0.138$ rad and assumes an isotropic phase function in the near-180° direction. Delta-Eddington scaling is used for the TDTS method.

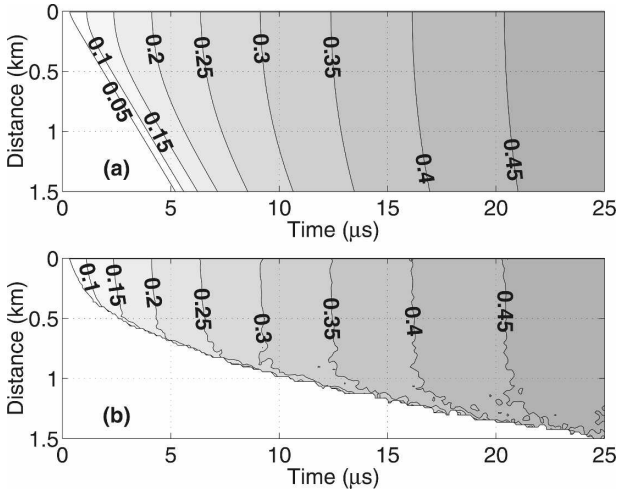

FIG. 7. As Fig. 6, but for the RMS horizontal deviation of photons from the lidar axis, in kilometers. In (a) (the TDTS model), the quantity shown is $\sqrt{(J^+ + J^-)/(I^+ + I^-)}$.

The results are shown in Fig. 8, where it can be seen that the apparent backscatter profile in the first 500 m is rather different than in Fig. 5. This is because the backscatter coefficient (proportional to the value of the phase function at $\theta = \pi$ in Fig. 4) is much less. This leads to a considerably smaller fraction of the returned photons originating from single scattering and small-angle multiple scattering (the component that is calculated using the PVC method); rather, the wide-angle multiple scattering is dominant (the component calculated using the TDTS method). The performance of the TDTS–PVC calculation is somewhat worse than in Fig. 5, probably because the Henyey–Greenstein phase function contains an unrealistically wide forward lobe that blends smoothly into the rest of the phase function, so there is a less obvious transition between small-angle scattering and wide-angle scattering. Furthermore, the assumption made in the PVC method that after several forward-scattering events the photon angles with respect to their initial trajectory will still be small is violated because of the relatively wide forward lobe of the

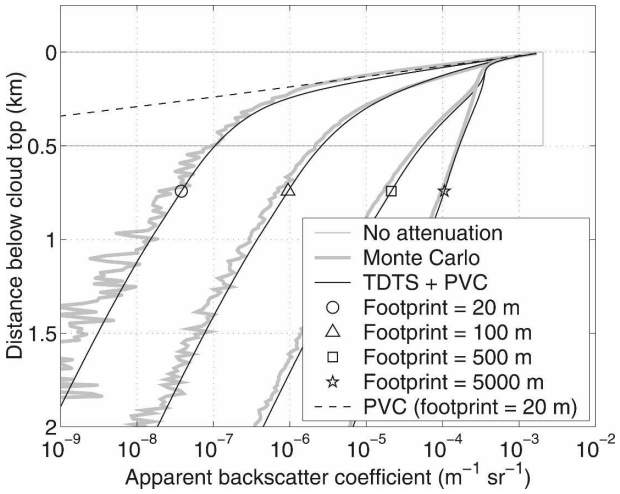

FIG. 9. As Fig. 5, but for the third profile described in section 5a (experiment 5 of I3RC; phase III, case 7) in which the cloud is 500 m thick and has an optical depth of 20; the scattering is described by the Mie phase function shown by the black solid line in Fig. 4.

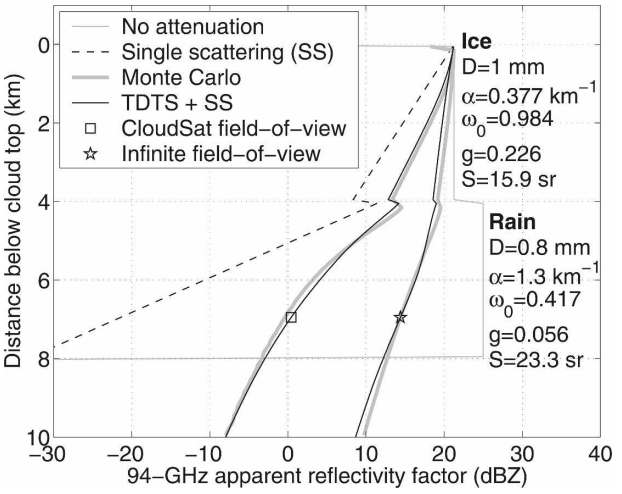

FIG. 10. Comparison of apparent radar reflectivity factor for the case described in section 5b. Note that D is particle diameter and S is extinction-to-backscatter ratio.

Henyey–Greenstein phase function. Note that the noise in the Monte Carlo calculations is due to the finite number of photons used.

The third profile (experiment 5 of I3RC; phase III, case 7) considers a nonabsorbing 500-m cloud of optical depth 20 with a more realistic phase function, described by Mie theory for a lognormal droplet-size distribution with an effective radius of 10 μm and a standard deviation that is 0.3 times the mean radius. The "equivalent-area radius" (required by the PVC method) for such a distribution is 11.96 μm. This is again modeled by a combination of the PVC and TDTS methods. Note that the PVC method is run assuming that the phase function is isotropic in the near-180° direction (but using the true backscatter coefficient taken from the peak in the phase function at 180°). Although the capability exists to represent anisotropic phase functions near backscatter (described in Part I), it has a small effect on the total apparent backscatter due to the dominance of wide-angle multiple scattering.

The results of the comparison are shown in Fig. 9, where it can be seen that the agreement within the cloud is much better than for the Henyey–Greenstein phase function. This is because there is a clear transition between the small-angle forward scattering (caused by the sharp forward lobe a few degrees from $\theta = 0$ in Fig. 4) and the wide-angle scattering. This is encouraging because the Mie phase function is much more similar to the phase functions of real clouds (liquid and ice) than Henyey–Greenstein for the same value of g. The backscatter profile in the topmost 50 m of the cloud is very different from that shown in both Figs. 5 and 8 because of the peak in the phase function in the near-180° direction, which enhances the small-angle multiple scattering return relative to the wide-angle return. It should be noted that in this case, because the cloud is vertically finite, the return from beyond an apparent distance of 500 m is entirely due to wide-angle multiple scattering.

b. Spaceborne radar

To evaluate the performance of the new multiple scattering model for a spaceborne 94-GHz radar, we use an idealized profile based on scenario 3 of Battaglia et al. (2008). This consists of a 4-km layer of 1-mm ice spheres overlying a 4-km layer of 0.8-mm raindrops, with the properties indicated to the right of Fig. 10; the corresponding phase functions are shown by the gray lines in Fig. 4. The total optical depth of the cloud is 6.7. The pulse length is 100 m and the radiation is unpolarized. The radar is at an altitude of 715 km and is assumed to have a Gaussian transmitter pattern with a 1/e half-angle beam divergence of $\rho_{tr} = 1.13$ mrad, similar to *CloudSat*. The reference dielectric factor in (1) is $|K_l|^2 = 0.75$.

Figure 10 compares the Monte Carlo model and the new model (using the sum of the TDTS and single scattering returns) for a receiver with the same Gaussian pattern as the transmitter (the *CloudSat* field of view) and an infinite field of view. Very good agreement is again observed. It should be noted that although this case is vertically inhomogeneous, in some regards it is rather less challenging than the lidar comparisons in the previous section: first, for particles smaller than the

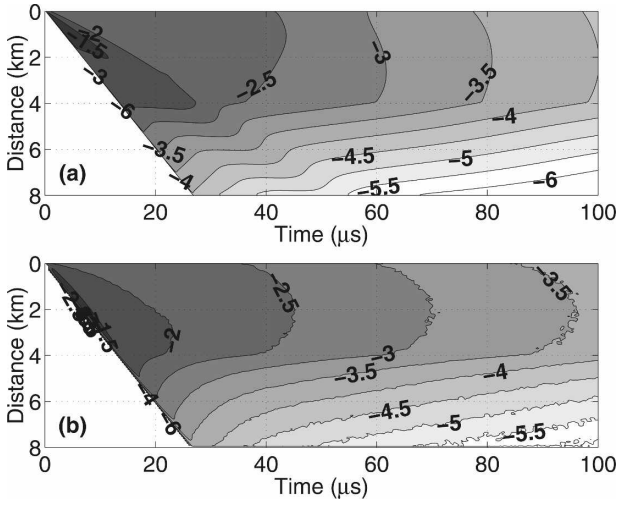

FIG. 11. The base-10 logarithm of the total diffuse radiative energy in a given level as a function of time and true distance below cloud top for the radar case shown in Fig. 10, calculated by (a) the TDTS model and (b) the Monte Carlo model.

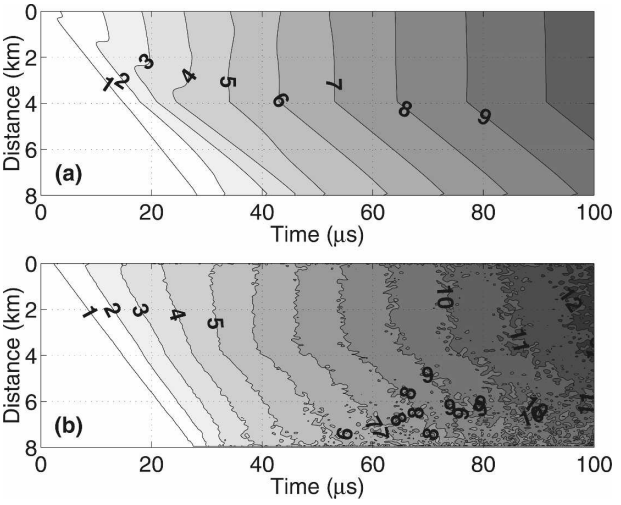

FIG. 12. As Fig. 11, but for the RMS horizontal deviation of the radiation from the radar axis, in kilometers.

wavelength, the phase function has a very simple shape, being nearly Rayleigh (see Fig. 4). Second, the transmitter has a Gaussian pattern and so after a few scattering events the distribution of radiation is still reasonably well described by a Gaussian, unlike for the point source in the I3RC cases.

Figures 11 and 12 compare the total energy and RMS horizontal displacement of the radiation within the cloud as a function of time and distance below cloud top. The diagonal edge to the left of each panel again corresponds to the incoming direct beam. Reasonable agreement is evident for both variables, although as time progresses there is a slight tendency for the TDTS model to underestimate both of them. A possible reason for this was given at the end of section 4b: if the radiation that escapes from the top of the cloud is preferentially that with a smaller spatial variance, then that which remains will tend to have a larger variance. Likewise, the remaining radiation will tend to be more directed in the horizontal than the vertical and so will tend to remain in the cloud for longer. Neither of these effects is currently represented in the TDTS model. There is also evidence for weak artifacts introduced by the two-stream approximation: both Figs. 11a and 12a exhibit kinks in the contours corresponding to a broad ray propagating out from the origin with a speed of $c/2$. However, these effects do not appear to have fed through significantly to the backscatter in Fig. 10.

6. Conclusions

A fast model has been described to calculate the time-dependent multiple-scattering returns from lidar or radar. It uses a hybrid approach, with the small-angle multiple-scattering returns characteristic of lidar being calculated by the photon variance–covariance (PVC) method (either as formulated in Part I or as formulated by Hogan 2006) and the wide-angle multiple scattering that occurs for both radar and lidar being calculated using the time-dependent two-stream (TDTS) approximation described here. Both components of the model are $O(N^2)$ efficient or better for an N-point profile. An intercomparison of the speeds of the various algorithms is given in Table 1. It can be seen that the execution time is typically on the order of milliseconds, making it particularly suitable for use as the forward model in spaceborne radar and/or lidar retrieval schemes in which a new profile is recorded approximately every 100 ms. It is also useful when taking the approach of evaluating the representation of clouds in climate and forecast models by forward-modeling the observed variables, something that has recently been done for the *CloudSat* radar (Haynes et al. 2007) and the *ICESat* lidar (Wilkinson et al. 2008).

Comparison of the new scheme against Monte Carlo shows encouragingly good agreement both for the variables describing the photon distribution versus time and range and for the final apparent backscatter profile. Poorer agreement is found for phase functions in which forward scattering is dominant but is not in a very narrow forward lobe (such as the Henyey–Greenstein phase function for $g = 0.85$), because then some of the assumptions made by the PVC method are violated. However, for both the more isotropic phase functions that are encountered by spaceborne radar and the narrow forward-peaked phase functions encountered by lidar in the large-particle limit, there is a

TABLE 1. Execution time of the various algorithms for a profile described by $N = 100$ cloudy points, relative to the time for the Hogan (2006) algorithm (which takes 1.9 ms on a 1-GHz Intel processor). The reported efficiency enables the time for any other number of points to be estimated. Relative execution times are reported to two significant figures and have been calculated from repeated calls to the core algorithm, thereby excluding any time associated with memory allocation and input/output of data. The $O(N)$ PVC method was described in Part I and its speed is reported here for both the standard implementation and the implementation taking into account the anisotropic phase function in the near-180°direction (assuming liquid droplets). The "explicit" method was outlined in Part I and separately calculates the contribution from each order of scattering (up to the indicated order) as in the Eloranta (1998) algorithm; the reported speed is found to be within 20% of Eloranta's algorithm for the same profile. The Monte Carlo model is that of Battaglia et al. (2006), the speed of which scales with the number of photons used and hence the accuracy; Battaglia et al. (2008) reported that 28×10^6 photons took 5 h to compute on a single 3-GHz Intel processor.

Algorithm	Efficiency	Relative time
Quasi-small-angle scattering		
PVC (Part I)	N	0.066
PVC (Part I, anisotropic)	N	0.10
PVC (Hogan 2006)	N^2	1.0
Explicit to 3rd order	N^3	23
Explicit to 4th order	N^4	590
Explicit to 5th order	N^5	62 000
Wide-angle scattering		
TDTS (this paper)	N^2	8.7
Monte Carlo	—	$\sim 10^7$

much more clear-cut division between small-angle and wide-angle multiple scattering, and the hybrid approach works well.

A number of developments of the TDTS model are planned. First, there is a need to find a fast method to estimate the Jacobian matrix (i.e., the derivative of the attenuated backscatter with respect to each of the input variables, in particular the extinction coefficient at each range gate). This is required if the model is to be used as part of a variational retrieval scheme (Rodgers 2000; L'Ecuyer and Stephens 2002; Delanoë and Hogan 2008). Second, a common feature of spaceborne lidar and radar observations is of multiply scattered cloud echoes appearing to originate from beneath the ground. To forward-model this phenomenon, it is necessary to include surface reflection in the model. This capability has recently been added to the Battaglia et al. (2006) Monte Carlo code, which will be used to test its implementation in the TDTS code. Third, a further piece of information available when multiple scattering occurs is from the depolarization ratio, because in a medium that normally does not depolarize (e.g., liquid water droplets observed by lidar), the effect of multiple scattering is to progressively depolarize the light such that, in principle, this variable provides information on the number of scattering events that have occurred (Sassen and Petrilla 1986). To interpret such measurements correctly, the capability to model the depolarization due to multiple scattering will be added to both the PVC and TDTS models.

The code for the algorithm is freely available for download from the lead author's web site (http://www.met.reading.ac.uk/clouds).

Acknowledgments. We thank Tamás Várnai for coordinating the I3RC intercomparisons and providing the Mie phase function shown in Fig. 4.

APPENDIX

Discretizing the Two-Stream Equations in Optically Thick Media

As discussed at the end of section 4a, for optically thick media (specifically those with $l_t \lesssim \Delta r$) a simple discretization of the time-dependent two-stream equations such as (14) is inaccurate and may be numerically unstable. A solution is to use the discretization given in (15), in which the coefficients Δ_i^0 to Δ_i^5 are precomputed at each gate i. These coefficients describe how an initial radiance $I_{i,j}^+$ (or $I_{i,j}^-$) at time step j is distributed among the outgoing and incoming radiances in the adjacent range gates at the subsequent time step $j + 1$. This appendix outlines how these coefficients are derived.

For simplicity, we assume that the properties of range gates $i + 1$ and $i - 1$ are the same as at gate i; this ensures that the Δ_i coefficients only depend on the properties at gate i. The photons that constitute the radiance $I_{i,j}^+$ are assumed to be traveling in the same direction $+\mu_1$. In a single time step $\Delta t = \Delta r/c$, the total distance traveled by an unabsorbed photon will be Δr. However, we are interested in the mean distance traveled in the direction toward or away from the instrument in a single time step. In the two-stream approximation, the maximum that this can be is $\mu_1 \Delta r$.

Our approach is semiempirical. First, high-resolution runs of the time-dependent two-stream method are performed to estimate the coefficients as a function of the optical depth within a single range gate, using the simple discretization of (14). In each simulation, a one-dimensional grid between $r = -\Delta r$ and $r = 2\Delta r$ is initialized with $I^+ = 1$ between $r = 0$ and $r = \Delta r$ and $I^+ = 0$ elsewhere; I^- is set to 0 everywhere. The high-resolution grid spacing $\Delta r'$ is chosen to ensure that the optical depth within a single high-resolution layer is less than 0.05. The simulation is run for time $\Delta t = \Delta r/c$, but

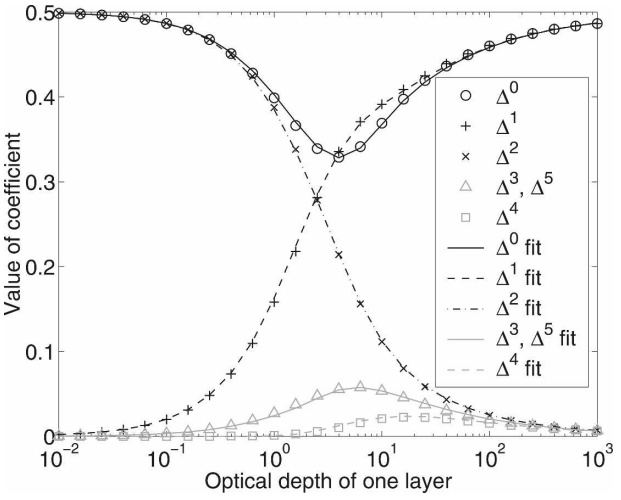

FIG. A1. Values of the coefficients introduced in (15) vs the optical depth of a single model level for a cloud with $\tilde{\omega} = 1$ and $g = 0.45$. The symbols are derived from a high-resolution run of the TDTS equations (as described in the appendix); the lines represent semiempirical fits to these points as described by (A1)–(A9). Note that this value of g corresponds to $g = 0.82$ after delta-Eddington scaling.

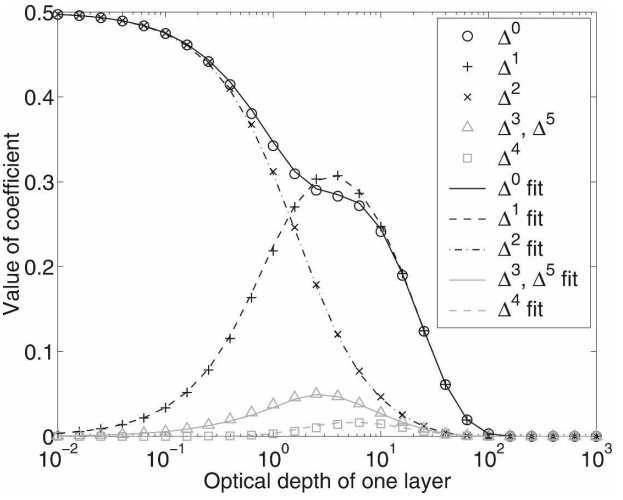

FIG. A2. As Fig. A1, but for $\tilde{\omega} = 0.95$ and $g = 0$.

using time steps of $\Delta t' = \Delta r'/c$. At the end of the simulation, the six coefficients are calculated as the fraction of the initial energy that has been transported to each of the two directions and three ranges of Δr in the domain. The results for $\tilde{\omega} = 1$ and $g = 0.45$ are shown by the symbols in Fig. A1 as a function of the optical depth of one layer. Figure A2 shows the same, but for a layer of partially absorbing isotropic scatterers.

The next step is to fit these computations analytically. When one attempts to calculate analytically the distance that radiation will be transported in the scenario described above, it becomes clear that four particular variables must be important. These variables are now derived. They are then combined to fit the modeled points indicated in Figs. A1 and A2, and heuristic arguments are presented to explain the analytical expressions.

The first variable is the fraction of photons that will remain unscattered after a single time step:

$$F_t = \exp(-\Delta r/l_t), \tag{A1}$$

where l_t is the transport mean-free path [see Eq. (18)]. The second variable is the fraction of photons that are unabsorbed (although they may be scattered) after a single time step:

$$F_a = \exp(-\Delta r/l_a), \tag{A2}$$

where $l_a = [\alpha(1 - \tilde{\omega})]^{-1}$ is the absorption mean-free path. Of those photons that are scattered before a time step has elapsed, the mean fraction of a range gate that has been traversed at the point of scattering provides our third variable, given by

$$L = \frac{1}{\Delta r}\int_0^{\Delta r} \mu_1 r \exp(-r/l_t)\, dr \Big/ \int_0^{\Delta r} \exp(-r/l_t)\, dr = \mu_1\left[\frac{l_t}{\Delta r} - \frac{F_t}{(1 - F_t)}\right]. \tag{A3}$$

Last, we consider the behavior in the optically thick limit when there are many scattering events within the time step. In this situation, diffusion theory may be applied, and the fraction of the radiation that diffuses from one layer to the next in a single time step provides the fourth variable:

$$L_d = \mu_1 F_a (l_t/3\Delta r)^{1/2}. \tag{A4}$$

The form of this expression can be explained as follows: (16) and (17) predict that in a time step the mean-squared displacement changes in proportion to $cl_t\Delta t = l_t\Delta r$, and hence the root-mean-square displacement in proportion to $\sqrt{l_t\Delta r}$. Because (A4) is the fraction of a range gate that has been traversed, we divide through by Δr and multiply by F_a to remove absorbed photons.

Expressions for the coefficients Δ_i^0 to Δ_i^5 are derived by assuming that the total transport from one gate and direction to another can be described by the sum of a nondiffusive component, which dominates in the optically thin limit and involves the first three variables, and a diffusive component, which dominates in the optically thick limit and involves the fourth variable. The nondiffusive transport component essentially describes the transport of photons that have some memory of their initial direction within a single time step. A combination of empirical fitting and physical insight was used

to derive the following fits to the points in Figs. A1 and A2:

$$\Delta^0 = F_1(1 - \mu_1) + (F_a - F_t)(1/2 - L) - L_d C_0, \tag{A5}$$

$$\Delta^1 = (F_a - F_1)(1 - L)/2 - L_d C_1, \tag{A6}$$

$$\Delta^2 = \mu_1 F_t + (F_a - F_t)L + L_d C_0/2, \tag{A7}$$

$$\Delta^3 = \Delta^5 = (F_a - F_t)L/4 + L_d C_1/2, \tag{A8}$$

$$\Delta^4 = L_d C_0/2, \tag{A9}$$

where the empirical terms scaling the diffusive transport are

$$C_0 = \exp[-3.7(l_t/\Delta r)^{3/4}], \tag{A10}$$

$$C_1 = \exp[-3.7(l_t/\Delta r)]. \tag{A11}$$

These two terms simply correct for the fact that at low optical depths ($l_t \ll \Delta r$), diffusion theory (expressed by L_d) predicts excessively high transport.

The nondiffusive transport terms (those involving F_a, F_t, and L) may be understood physically. For example, consider Δ^2, which describes the transport from one gate to the next in the same direction. The first term on the right-hand side of (A7) expresses the fact that in one time step, some fraction F_t of the photons are not scattered or absorbed, so they travel a further fraction μ_1 of a range gate. The second term states that an additional fraction $F_a - F_t$ of the photons are scattered after traveling a fraction L of a range gate, on average. Similar arguments may be used to understand the other nondiffusive transport terms.

An alternative approach to the above would be to employ the Langevin equation [used in the derivation of Eq. (19)] to provide a more physical basis for the transport in the transition between ballistic and diffusive behavior.

REFERENCES

Ayoubi, I. S., and P. Nelson, 1989: Concentration profiles from lidar measurements in the presence of multiple scattering: The two-stream approximation. *Appl. Opt.,* **28,** 4133–4140.

Battaglia, A., M. O. Ajewole, and C. Simmer, 2006: Evaluation of radar multiple scattering effects from a GPM perspective. Part I: Model description and validation. *J. Appl. Meteor. Climatol.,* **45,** 1634–1647.

——, ——, and ——, 2007: Evaluation of radar multiple scattering effects in CloudSat configuration. *Atmos. Chem. Phys.,* **7,** 1719–1730.

——, S. Kobayashi, S. Tanelli, C. Simmer, and E. Im, 2008: Multiple scattering effects in pulsed radar systems: An intercomparison study. *J. Atmos. Oceanic Technol.,* **25,** 1556–1567.

Cahalan, R. E., M. McGill, J. Kolasinski, T. Várnai, and K. Yetzer, 2005a: THOR—Cloud thickness from offbeam lidar returns. *J. Atmos. Oceanic Technol.,* **22,** 605–627.

——, and Coauthors, 2005b: The I3RC: Bringing together the most advanced radiative transfer tools for cloudy atmospheres. *Bull. Amer. Meteor. Soc.,* **86,** 1275–1293.

Davis, A. B., and A. Marshak, 2001: Multiple scattering in clouds: Insights from three-dimensional diffusion/P_1 theory. *Nucl. Sci. Eng.,* **137,** 251–280.

——, and ——, 2002: Space–time characteristics of light transmitted through dense clouds: A Green's function analysis. *J. Atmos. Sci.,* **59,** 2713–2727.

——, R. F. Cahalan, J. D. Spinhirne, M. J. McGill, and S. P. Love, 1999: Off-beam lidar: An emerging technique in cloud remote sensing based on radiative Green-function theory in the diffusion domain. *Phys. Chem. Earth,* **24B,** 177–185; Erratum, 757–765.

Delanoë, J., and R. J. Hogan, 2008: A variational scheme for retrieving ice cloud properties from combined radar, lidar and infrared radiometer. *J. Geophys. Res.,* **113,** D07204, doi:10.1029/2007JD009000.

Donovan, D. P., and Coauthors, 2001: Cloud effective particle size and water content profile retrievals using combined lidar and radar observations. 2. Comparison with IR radiometer and in situ measurements of ice clouds. *J. Geophys. Res.,* **106,** 27 449–27 464.

Durduran, T., A. G. Yodh, B. Chance, and D. A. Boas, 1997: Does the photon-diffusion coefficient depend on absorption? *J. Opt. Soc. Amer.,* **14A,** 3358–3365.

Durian, D. J., and J. Rudnick, 1997: Photon migration at short times and distances and in cases of strong absorption. *J. Opt. Soc. Amer.,* **14A,** 235–245; Erratum, 940.

Edwards, J. M., and A. Slingo, 1996: Studies with a flexible new radiation code. 1. Choosing a configuration for a large-scale model. *Quart. J. Roy. Meteor. Soc.,* **122,** 689–719.

Einstein, A., 1956: *Investigations on the Theory of the Brownian Movement.* Dover, 119 pp.

Eloranta, E. W., 1998: A practical model for the calculation of multiply scattered lidar returns. *Appl. Opt.,* **37,** 2464–2472.

Gopal, V., S. Anantha Ramakrishna, A. K. Sood, and N. Kumar, 2001: Photon transport in thin disordered slabs. *Pramana J. Phys.,* **56,** 767–778.

Haynes, J. M., R. T. Marchand, Z. Luo, A. Bodas-Salcedo, and G. L. Stephens, 2007: A multipurpose radar simulation package: QuickBeam. *Bull. Amer. Meteor. Soc.,* **88,** 1723–1727.

Hogan, R. J., 2006: Fast approximate calculation of multiply scattered lidar returns. *Appl. Opt.,* **45,** 5984–5992.

——, 2008: Fast lidar and radar multiple-scattering models. Part I: Small-angle scattering using the photon variance–covariance method. *J. Atmos. Sci.,* **65,** 3621–3635.

——, M. P. Mittermaier, and A. J. Illingworth, 2006: The retrieval of ice water content from radar reflectivity factor and temperature and its use in evaluating a mesoscale model. *J. Appl. Meteor. Climatol.,* **45,** 301–317.

Ito, S., S. Kobayashi, and T. Oguchi, 2007: Multiple-scattering formulation of pulsed beam waves in hydrometeors and its application to millimeter-wave weather radar. *IEEE Geosci. Remote Sens. Lett.,* **4,** 13–17.

Joseph, J. H., W. J. Wiscombe, and J. A. Weinman, 1976: The delta-Eddington approximation for radiative flux transfer. *J. Atmos. Sci.,* **33,** 2452–2459.

Kobayashi, S., T. Oguchi, S. Tanelli, and E. Im, 2006: Backscattering enhancement on spheroid-shaped hydrometeors: Considerations in water and ice particles of uniform size and

Marshall–Palmer distributed rains. *Radio Sci.,* **42,** RS2001, doi:10.1029/2006RS003503.

L'Ecuyer, T. S., and G. L. Stephens, 2002: An estimation-based precipitation retrieval algorithm for attenuating radars. *J. Appl. Meteor.,* **41,** 272–285.

Meador, W. E., and W. R. Weaver, 1980: Two-stream approximations to radiative transfer in planetary atmospheres: A unified description of existing methods and a new improvement. *J. Atmos. Sci.,* **37,** 630–643.

Platnick, S., 2001: Approximations for horizontal photon transport in cloud remote sensing problems. *J. Quant. Spectosc. Radiat. Transfer,* **68,** 75–99.

Platt, C. M. R., 1981: Remote sounding of high clouds. III: Monte Carlo calculations of multiple-scattered lidar returns. *J. Atmos. Sci.,* **38,** 156–167.

——, and D. M. Winker, 1995: Multiple scattering effects in clouds observed from LITE. *Optics in Atmospheric Propagation and Adaptive Systems,* A. Kohnle, Ed., International Society for Optical Engineering (SPIE Proceedings, Vol. 2580), 60–71.

Polonsky, I. N., S. P. Love, and A. B. Davis, 2005: Wide-angle imaging lidar deployment at the ARM Southern Great Plains site: Intercomparison of cloud property retrievals. *J. Atmos. Oceanic Technol.,* **22,** 628–648.

Rodgers, C. D., 2000: *Inverse Methods for Atmospheric Sounding: Theory and Practice.* World Scientific, 238 pp.

Sassen, K., and R. L. Petrilla, 1986: Lidar depolarization from multiple scattering in marine stratus clouds. *Appl. Opt.,* **25,** 1450–1459.

Shonk, J. K. P., and R. J. Hogan, 2008: Tripleclouds: An efficient method for representing cloud inhomogeneity in 1D radiation schemes by using three regions at each height. *J. Climate,* **21,** 2352–2370.

Stephens, G. L., P. M. Gabriel, and P. T. Partain, 2001: Parameterization of atmospheric radiative transfer. Part I: Validity of simple models. *J. Atmos. Sci.,* **58,** 3391–3409.

Toon, O. B., C. P. McKay, T. P. Ackerman, and K. Santhanam, 1989: Rapid calculation of radiative heating rates and photodissociation rates in inhomogeneous multiple scattering atmospheres. *J. Geophys. Res.,* **94,** 16 287–16 301.

Uhlenbeck, G. E., and L. S. Ornstein, 1930: On the theory of the Brownian motion. *Phys. Rev.,* **36,** 823–841.

Wilkinson, J. M., R. J. Hogan, A. J. Illingworth, and A. Benedetti, 2008: Use of a lidar forward model for global comparisons of cloud fraction between the ICESat lidar and the ECMWF model. *Mon. Wea. Rev.,* **136,** 3742–3759.

Zdunkowski, W. G., W.-G. Panhans, R. M. Welch, and G. J. Korb, 1982: A radiation scheme for circulation and climate models. *Beitr. Phys. Atmos.,* **55,** 215–238.